

PPPL-5267

## Electron temperature profile measurements using variable energy x-ray detection

J. Maddox, L. Delgado-Aparicio, N. Pablant, K.W. Hill, M. Bitter, J. E. Rice, M.L. Reinke, A. Hubbard, P. Efthimion, B. Stratton, S. Wolfe

July 2016



Prepared for the U.S. Department of Energy under Contract DE-AC02-09CH11466.

# Princeton Plasma Physics Laboratory

## Report Disclaimers

---

### Full Legal Disclaimer

This report was prepared as an account of work sponsored by an agency of the United States Government. Neither the United States Government nor any agency thereof, nor any of their employees, nor any of their contractors, subcontractors or their employees, makes any warranty, express or implied, or assumes any legal liability or responsibility for the accuracy, completeness, or any third party's use or the results of such use of any information, apparatus, product, or process disclosed, or represents that its use would not infringe privately owned rights. Reference herein to any specific commercial product, process, or service by trade name, trademark, manufacturer, or otherwise, does not necessarily constitute or imply its endorsement, recommendation, or favoring by the United States Government or any agency thereof or its contractors or subcontractors. The views and opinions of authors expressed herein do not necessarily state or reflect those of the United States Government or any agency thereof.

### Trademark Disclaimer

Reference herein to any specific commercial product, process, or service by trade name, trademark, manufacturer, or otherwise, does not necessarily constitute or imply its endorsement, recommendation, or favoring by the United States Government or any agency thereof or its contractors or subcontractors.

---

## PPPL Report Availability

### Princeton Plasma Physics Laboratory:

<http://www.pppl.gov/techreports.cfm>

### Office of Scientific and Technical Information (OSTI):

<http://www.osti.gov/scitech/>

---

### Related Links:

[U.S. Department of Energy](#)

[U.S. Department of Energy Office of Science](#)

[U.S. Department of Energy Office of Fusion Energy Sciences](#)

# Electron temperature profile measurements using variable energy x-ray detection

J. Maddox<sup>1</sup>, L. Delgado-Aparicio<sup>1</sup>, N. Pablant<sup>1</sup>, K.W. Hill<sup>1</sup>, M. Bitter<sup>1</sup>, J. E. Rice<sup>2</sup>, M.L. Reinke<sup>3</sup>, A. Hubbard<sup>2</sup>, P. Efthimion<sup>1</sup>, B. Stratton<sup>1</sup> and S. Wolfe<sup>2</sup>

<sup>1</sup>PPPL, 100 Stellarator Rd, Princeton, NJ 08540, USA

<sup>2</sup>MIT-PSFC, NW-17, 175 Albany St, Cambridge, MA 02139, USA

<sup>3</sup>Oak Ridge National Laboratory, 1 Bethel Valley Rd, Oak Ridge, TN 37831, USA

E-mail: jmaddox@pppl.gov

**Abstract.** By using a multi-energy soft x-ray (ME-SXR) diagnostic, simultaneous measurements of a variety of plasma parameters is demonstrated for magnetically confined fusion (MCF) plasmas. A prototype installed at C-Mod uses a Pilatus2 2D pixelated x-ray detector in which each individual pixel has a user-controlled minimum-energy threshold, with 13 energy threshold levels between 4 keV and 16 keV, at 1 keV intervals. Characteristic line-emission from medium and high-Z impurities can be isolated using appropriate energy thresholds. Detection of soft x-ray continuum intensities in line-free regions at different energy thresholds allows an line-integrated electron temperature to be deduced from the dependence of continuum emission with photon energy. The electron temperature is measured in a variety of plasma conditions with temporal resolution of 10 ms and spatial resolution of approximately 3 cm, and is in reasonable agreement with electron cyclotron emission (ECE) electron temperature measurements.

## 1. Motivation

$$S_{Det} = (I_{line} + a_{line} Shr(x_{trm} - Trm_{line})) \operatorname{erfc}\left(\frac{(x_{trm} - Trm_{line})}{\sqrt{2} Trm_{width_{line}}}\right) / 2 + I_{oth} \operatorname{erfc}\left(\frac{(x_{trm} - Trm_{oth})}{\sqrt{2} Trm_{width_{oth}}}\right) / 2 + a_{background} + a_{back} Shr(x_{trm} - Trm_{line}). \quad (1)$$

Here data from a novel PILATUS2 x-ray detector is used to infer electron temperature by making a fit of expected continuum radiation versus photon energy. In the future, this approach will be able to simultaneously measure electron temperature profiles and medium and high-Z impurities densities, as well as probe the product of the effective charge and electron density ( $Z_{eff}n_e^2$ ) profiles, and the emergence of fast supra-thermal electrons, ( $n_{e,fast}$ ). The technique is suitable for all plasmas at high enough temperatures to generate sufficient bremsstrahlung and line radiation in the energy range of interest. The multi-energy soft x-ray (ME-SXR) detector records line of sight brightness profiles of x-ray counts which can be tomographically inverted to obtain local emissivities. State of the art x-ray detection technology allows for the measurement of essential plasma parameters by sampling the continuum and impurity line emission. High-Z plasma facing components (PFCs) have x-ray spectra with line-free regions at soft x-ray energies allowing ME-SXR analysis to probe electron temperatures ( $T_e$ ) in reactors with metal PFCs. Plasma profiles dominated by line-emission processes ( $\propto n_Z$ ) from medium- to high-Z impurities can also be obtained using appropriate detector thresholds.

Magnetically confined plasmas in ITER and beyond will require diagnostics of electron temperature  $T_e$ , and impurity ( $n_Z$ ) and electron ( $n_e$ ) density profiles. Diagnostics in a burning fusion reactor must be protected from microwave and gamma radiation, as well as a strong neutron flux from D-D and D-T fusion reactions. Plasmas reaching temperatures greater than 10 keV become increasingly relativistic and electron cyclotron emission (ECE) and Thomson scattering (TS) measurements must be continually corrected [1, 2, 3]. Moreover, the use of radio frequency (RF) current drive techniques, such as Lower Hybrid Current Drive (LHCD), can lead to electrons in non-Maxwellian electron distributions leaving ECE measurements difficult to interpret due to a downshift of the electron gyro-frequency ( $\Omega = eB/\gamma m_e$ ) [2, 4]. The ME-SXR system presents the possibility of a compact solution to circumvent these challenges. In particular, ME-SXR diagnostics can observe the effects introduced by a non-thermal electron population but not in a manner which perturbs the slope of the continuum emission at low-energies, still allowing for an assessment of  $T_e$  and  $n_e^2 Z_{eff}$  profiles as mentioned above.

The paper describes the recent measurements obtained from a multi-energy soft x-ray (ME-SXR) system using a PILATUS2 detector installed at the Alcator C-Mod tokamak<sup>2</sup>. The data set presented was obtained using Ohmic and RF-heated plasmas in both low- and high-confinement discharge scenarios. Section 2 presents the description of background work aiming to determine electron temperature profiles using x-ray continuum radiation. Section 3 details the spectra of the most common medium- and high-Z impurities in C-Mod including both continuum and line emission processes. Section 4 overviews the detection chain and the basis of the temperature analysis. Section 5 details the brightness data taken by the detector at different thresholds and how the brightness profiles qualitatively relate to the density and temperature profiles. Section 6 overviews the determination of electron temperatures from those results and uses those methods for the duration of the plasma shot and across the different sight-lines of the detector. Section 7 outlines future work with this method to determine local temperatures, using tomographic inversion, deducing electron and impurity density and effective plasma charge profiles ( $Z_{eff}$ ), and the use of the technique at higher temperatures and with tungsten PFCs.

## 2. Background

Multi-energy x-ray systems have used a variety of detection options: from individual Silicon-Lithium [Si(Li)] detectors [5], a combination of scintillators, fiber optics and photomultiplier tubes [6], as well as diode-based systems [7, 8, 9]. These have generally fallen into two categories - detectors in photon-counting mode like Si(Li) or Silicon Drift Detectors (SDD) which have good energy resolution ( $\sim 0.1$  keV) but lack spatial resolution [5], or broadband detectors in current-mode which have good spatial resolution but poor energy resolution ( $\sim 2.0 - 5.0$  keV, depending on the foil characteristics) [6, 7, 10, 11]. In both cases the measurements are done along individual or multiple sightlines which allows for a coarse or fine tomographic reconstruction. The use of compact Absolute eXtreme Ultraviolet AXUV-diode arrays have facilitated

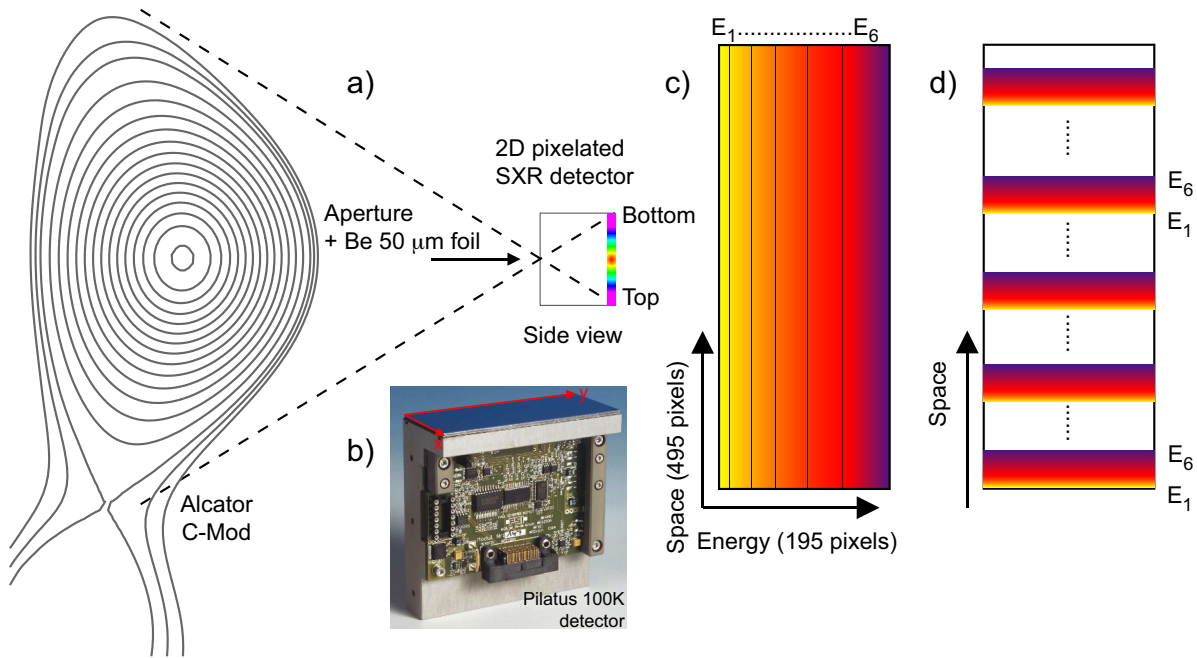


**Figure 1.** (Color Online) Inset (a) artist illustration schematic of the detector setup at Alcator C-Mod, (b) shows the detector used to collect the data of x-ray counts. Inset (c) shows a horizontal arrangement of the energy thresholds useful for applying the technique to the tangential line of sight (avoiding the center stack) not used in this paper, (d) shows a threshold configuration similar to that used in this paper.

the construction of ME-SXR systems worldwide. Good examples are the diagnostics installed at the Reversed Field Pinch (RFP) experiments in RFX and MST in Italy and USA respectively [8, 9], the TJII stellarator in Spain [12], and the core and edge systems installed at NSTX [7], NSTX-U, and EAST [13]. However, all these systems have very broad energy response due to the use of metallic filters which energy resolution inversely related to photon energy.

The multi-energy technique is in-between the pros and cons of the PHA and diode systems; ME-SXR has better energy resolution than diodes but worse temporal resolution and better temporal resolution than PHA but worse energy resolution. The PILATUS2 allows the user to set uniform detector energy thresholds with energy widths approximately independent of the energy of the threshold set. Each pixel of the detector has a maximum counting rate of 1-2 MHz per pixel and customizable energy thresholds for each of the  $\sim 100,000$  pixels [14]. These features resolve the also poor energy resolution and variable energy width inherent to foil and diode detector systems. Figure 1-a) shows a schematic of the installation at the Alcator C-Mod tokamak with a radial-view imaging the entire 2-D poloidal cross section and -b) depicts the  $24 \text{ cm}^2$  detector which is used.

Two possible arrangements of detector energy thresholds used in tangential or poloidal configurations are shown in Figures 1-c) and -d), respectively. Other configurations allow for for taking 2D images, which are ideal for tangential imaging [14]. The ability to set energy thresholds at arbitrary energies with constant energy resolution (e.g. 0.6 keV) is a significant improvement over metallic foil systems which have energy widths proportional to the energy characteristic 50% transmission. The ratios between soft x-ray intensities or brightnesses at different thresholds can then be used to obtain electron temperature profiles. Filtering bound-bound emission lines from known medium- to high-Z impurities is possible using using appropriate energy threshold settings. This process is particularly important in devices with metal plasma facing components which introduce impurities that are not fully stripped of electrons and thus emit significant line radiation.

Channels or lines-of-sight on the PILATUS2 detector were arranged for thirteen different energy thresholds, one per each row, 4-16 keV. Considering a  $197 \times 487$  array of pixels [15], this leaves 37 different chords (from the floor of  $487/13 = 37$ ) or lines of sight to deduce the plasma emissivity and the local electron temperatures. Each  $172 \times 172 \mu\text{m}^2$  pixel works by absorbing photons and counting them based on the photon's energy and the pixel's energy threshold setting. The likelihood of being absorbed by the  $320 \mu\text{m}$  thick silicon slab depends on photon energy. When absorbed, a photon excites a number of electrons, depending on its energy, to the band gap of n-doped-Si, creating a potential difference. A detection or count occurs if the energy of the photon is strong enough to excite an adequate potential difference. This difference is set by the user inputted energy thresholds [15].

### 3. Impurity Emissions

To isolate continuum radiation it is necessary to filter-out strong emission from bound-bound transitions from medium- to high-Z impurities. The most common x-ray emitting impurities in Alcator C-Mod are argon ( $Z=18$ ), which is introduced in trace amounts as a plasma diagnostic, and molybdenum ( $Z=42$ ), from the plasma facing components [16, 17]. Shown in Figures 2 and 3 are the spectra of Ar and Mo in the energy ranges of 1-25 keV, and a 'zoom' between 1 and 7 keV, respectively, as calculated by the FLYCHK code [18]. In the current configuration most of the detector energy thresholds are set inside an energy window which avoids medium- and high-Z impurity line-emission; only a few detector rows are able to detect the lower energy characteristic line-emission which will facilitate the impurity density measurement. In C-Mod plasmas, Ti, Fe, Cu, Ni have been observed transiently which allows for tests of the robustness of the Me-SXR technique since these impurities do have line emission in the 6-15 keV energy range. The detector response thresholds

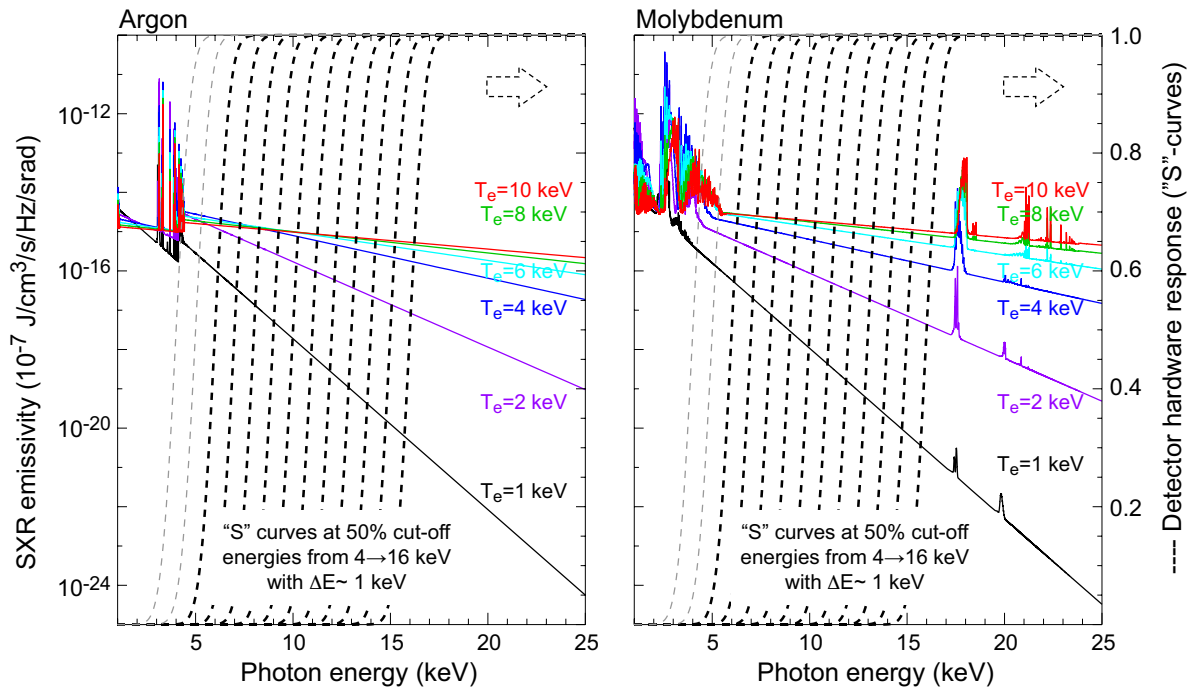


**Figure 2.** (Color Online) Spectra of soft x-ray emissivity from 0 to 25 keV, for electron temperatures ranging from 1 to 10 keV [18]. Energy thresholds are set by the detector response 'S'-curves shown by the dotted lines [14].

or energy thresholds are set between 4 and 16 keV, at 1 keV intervals as shown with the dotted lines in Figures 2 and 3.

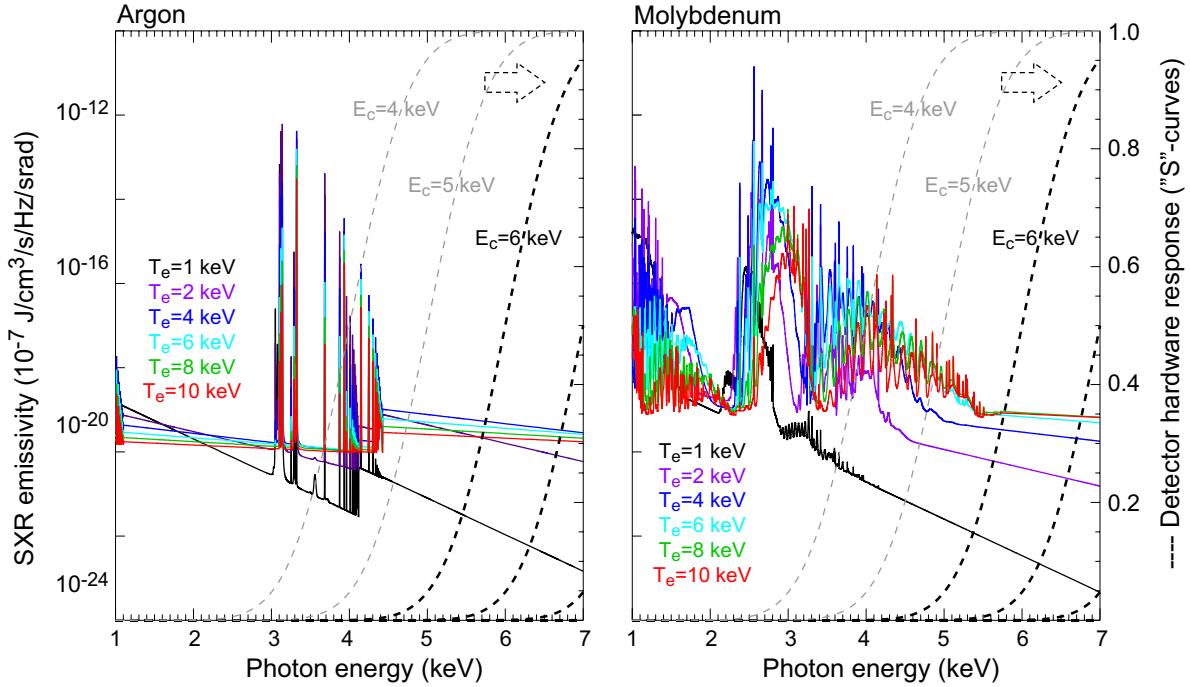


**Figure 3.** (Color Online) ‘Zoom-in’ on the above spectra from 1 to 7 keV, for temperatures ranging from 1 to 10 keV [18]. The 6 keV threshold is the first to be free of line emissions from Mo and Ar, or the Ar recombination edge. The ‘S’-curve width is approximately 0.6 keV regardless of the energy threshold; this presents a great advantage over the use of filters where the width of the threshold increases with energy [14].

Since argon and molybdenum impurities have a line-free continuum ‘window’ between 6-15 keV the detector rows with these energy thresholds are used to diagnose electron temperature. The photon counts obtained in between 4 and 6 keV and above 16 keV can be used to infer the relative concentrations of Ar and Mo, respectively. Other potential impurities such as iron (from the vacuum vessel and non-plasma facing components) and copper (from RF antennae) - which do have lines in the 6-15 keV range - were seen to be below the trace-limit from the spectroscopic data and therefore are not considered in this analysis.

## 4. Method of Analysis

The number of x-rays from bremsstrahlung emission detected depends on the local density ( $n_e$ ) and temperature ( $T_e$ ) of the plasma, the ‘mix’ of low-, medium- and high-Z impurities which define the plasma charge ( $Z_{eff}$ ) and the details of the detection-chain.

$$\mathcal{N}_{x-ray} = \frac{C n_e^2 Z_{eff}}{T_e^{1/2}} \int_0^\infty \frac{\exp(-E/T_e)}{E} \mathcal{T}_{Be} \mathcal{T}_{Air} \mathcal{A}_{Si} \mathcal{S}_{Det} dE. \quad (2)$$

An example of the energy dependence of the terms inside the integral is shown in Figure 4. The number of photons detected is proportional to the transmission product of air and the Be-filter ( $\mathcal{T}_{Be} \mathcal{T}_{Air}$ ), the x-ray absorption in the silicon lattice ( $\mathcal{A}_{Si}$ ), and the detector response ( $\mathcal{S}_{det}$ ). The constant factor  $C$  includes the geometry of the detector (e.g. ‘etendue’) and a line-averaged Gaunt-factors which are taken to be constant [19]. This assumption contributes to a systematic error due to the 10% variation of the gaunt free-free factor assuming a  $Z_{eff} \approx 3$ . These effects become important with larger impurity ion densities, particularly of high-Z. Moving forward with these assumptions, equation

(3) gives the transmission as a function of photon energy [11],

$$\mathcal{T}_{elem} = \exp(-E_0^3/E^3), \quad (3)$$

$$E_0 = (2Nr_0hc\tau k^2)^{1/3} = [\ln(2)]^{1/3} E_{C,50\%}.$$

The characteristic term  $E_0$  is given by the thickness of the material ( $\tau$ ), atomic density ( $N$ ), and energy scaling factor  $k$  comes from the energy dependence of the photons interaction with the atomic lattice [11];  $E_0$  is proportional to the photon energy at which the material transmits 50% of the incoming photons,  $E_{C,50\%}$  [6], as obtained from the x-ray transmission values measured by the Center for X-ray Optics [20]. Given the known thickness,  $\tau$ , of each medium (Be, air, Si), equation (3) models the attenuation of x-rays as they pass through each material from the plasma and what percentage are absorbed by the silicon detector,  $\mathcal{A}_{Si} = 1 - \mathcal{T}_{Si}$ . The  $S_{det}$  curve, in Figure 4, models the electrical response

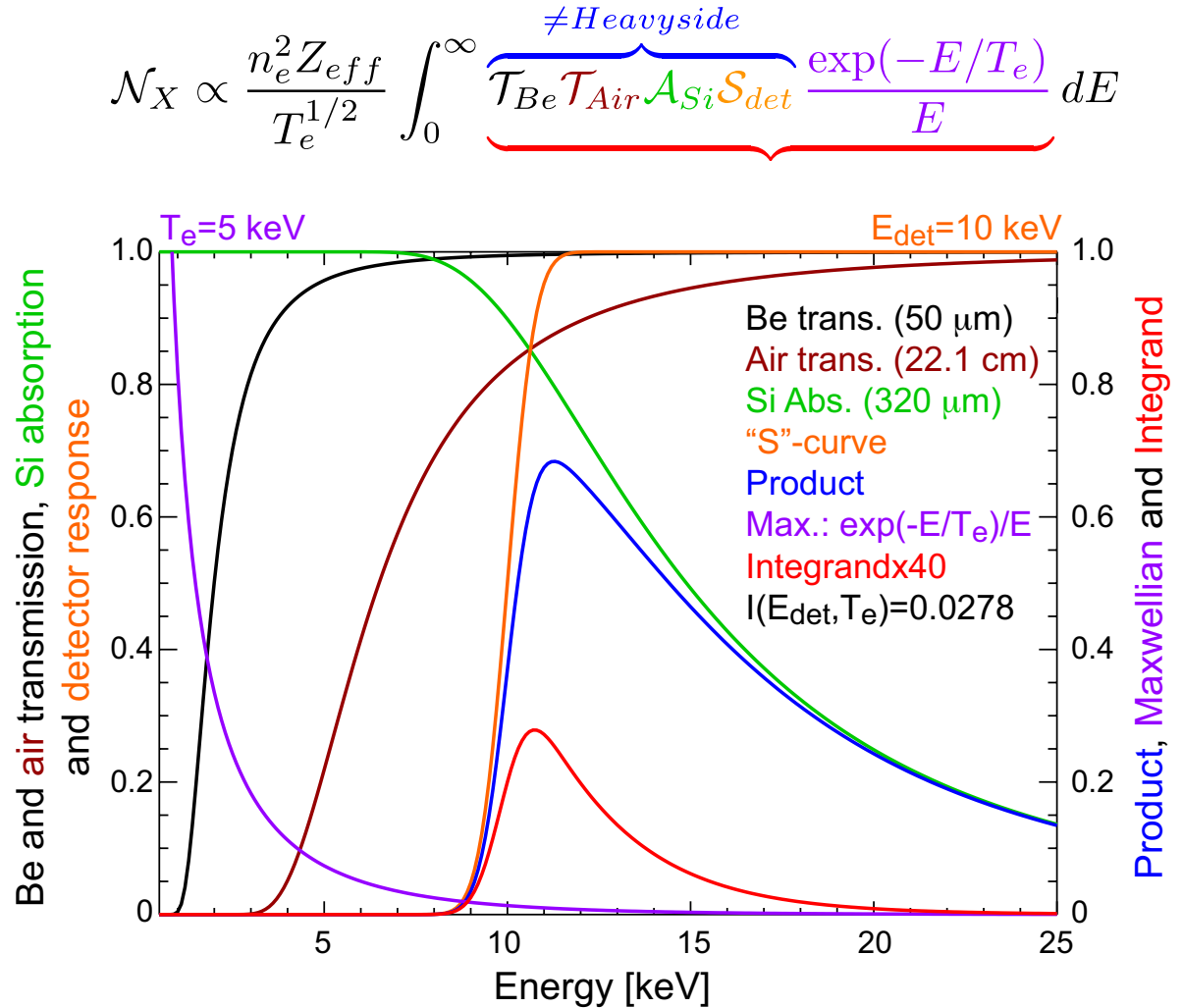


**Figure 4.** (Color Online) The transmission terms particular to the setup at Alcator C-Mod from equation (2) are shown inside the integral relating the number of bremsstrahlung photons detected to plasma conditions (purple, at 5 keV electron temperature) and detector energy threshold (orange, 10 keV example). Each term is plotted on the graph as a function of photon energy. The product of these terms is shown in red.

of the detector for each energy threshold. From the detector calibration, the detector efficiency for each energy threshold

can be fitted using the complementary error function of  $E_c$ , seen in equation (4) [14].

$$S_{Detc} = \text{erfc}\left(\frac{-(E - E_c)}{\sqrt{2}E_{width}}\right)/2. \quad (4)$$

In addition to the numerical solution for bremsstrahlung photons we make use of two ideal solutions, commonly used, which neglect the transmission and absorption and treats the detection chain with a Heavyside function at the minimum energy threshold. The ‘ideal’ solutions for the number of x-ray photons and the integrated x-ray power from bremsstrahlung are seen below in equations (5) and (6). Because these equations can be solved analytically they are useful to bound the numeric solution [11].

$$\mathcal{N}_{x\text{-ray}}^{ideal} = \frac{Cn_e^2 Z_{eff}}{T_e^{1/2}} \int_{E_{det}}^{\infty} \frac{\exp(-E/T_e)}{E} dE \propto E_1(E_{det}/T_e), \quad (5)$$

$$\mathcal{P}_{x\text{-ray}}^{ideal} = \frac{Cn_e^2 Z_{eff}}{T_e^{1/2}} \int_{E_{det}}^{\infty} \exp(-E/T_e) dE \propto T_e \exp(-E_{det}/T_e). \quad (6)$$

Where  $E_1$  is the exponential integral of the first order. By using a multiple least squares fitting routine considering the available energy ranges and we can fit the data with an electron temperature using equations (2), (5), and (6). The fits to data do not consider the brightness measurements using detector thresholds at 4 and 5 keV due to line-contamination from Ar and Mo, including the Ar recombination edge between 4 and 4.5 keV shown in Fig. 3-a) [5].

Multiple energy threshold settings on the detector allow for a measurement of the continuum’s dependence on photon energy which is strongly dependent on electron temperature [21]. The photons detected allow for the temperature dependent expression in equation (2) can be solved up to a constant. However, this formulation only accounts for constant gaunt factor continuum emissions, so atomic bound-bound and recombination edges will disrupt the counts to electron temperature analysis [5]. From equation (2) it can be seen that as the detector threshold energy varies the number of photons detected changes only as a strong function of electron temperature. In cases where bremsstrahlung dominates, such as when impurity concentrations are sufficiently low, the electron temperature calculated from the ratios of bremsstrahlung can also be used to calculate the profiles of  $n_e^2 Z_{eff}$ .

The dependence of the integrand in equation (1) with various detector thresholds at three plasma temperatures of 1, 2 and 5 keV is depicted in Figure 5. The total bremsstrahlung emission detected is proportional to the area under each curve and exhibits the importance of the exponential ratio of the photon energy and the local electron temperature. Because the relative area of each energy threshold’s curve changes so rapidly, the values of the electron temperature are very sensitive to the inferred ‘best’ fit between the available data and the numerical solutions of equation (1).

## 5. Results

The data presented in this paper was obtained in error-field-induced locked-mode experiments at Alcator C-Mod during Ohmic and ion cyclotron resonance heating (ICRH) scenarios. The typical plasma discharge parameters were  $R_0 \simeq 0.683$  m,  $a = .206$  m,  $I_p \simeq 0.8$  MA,  $B_{t,0} \simeq 5.4$  T,  $q_{95} \sim 4$ , with central electron temperature and densities of 2.0 keV and  $(0.6 - 1.3) \times 10^{20} \text{ m}^{-3}$ . Results from these experiments are shown in Figure 6; for this case, ICRH was applied during the current ramp-up of the error-field control coils. For  $P_{ICRH} > 1$  MW the plasma experienced L  $\rightarrow$  H transitions as the average density, core electron temperature, and stored energy increased up to  $2 \times 10^{20} \text{ m}^{-3}$ , 2-2.5 keV, and 150 kJ, respectively [see ‘peaked’ features in Figure 6-a)].

The data depicted in Figures 6-a) shows the time history of the total x-ray counts detected during the nearly two-second discharge. The insets in Figure 6-b) and -c) depict the brightness profiles at thirteen energy ranges at two times in the plasma discharge during low- and high-confinement (L- and H-modes). The space separating each of the 37 chords is 2.4-2.8 cm. The energy thresholds are separated by 1 keV with an approximate 10 – 90% threshold width

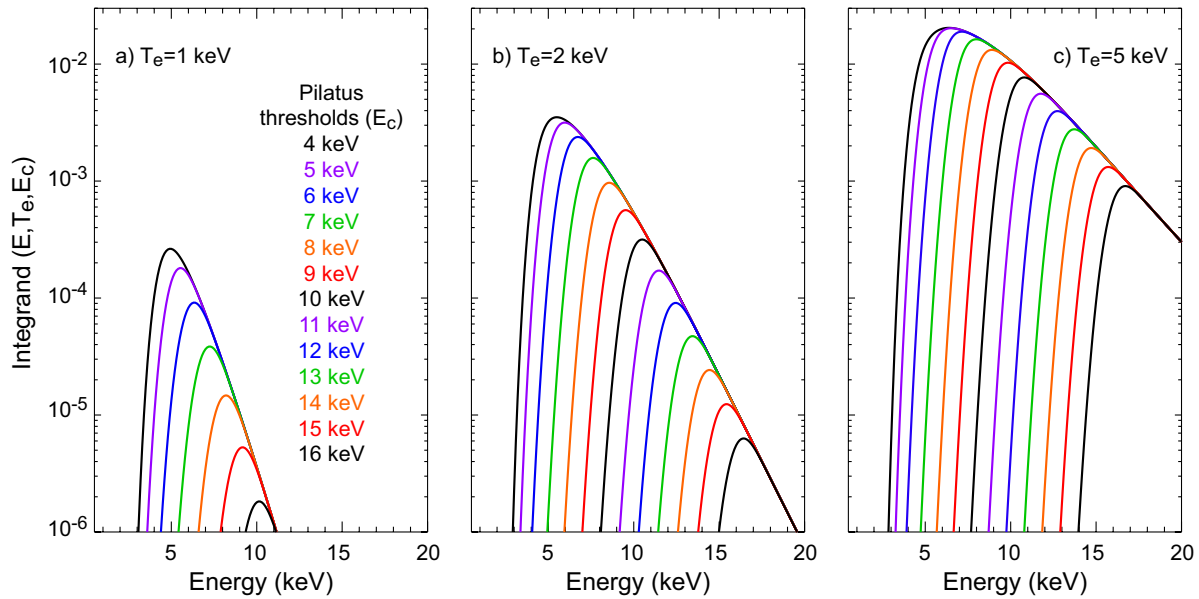


**Figure 5.** (Color Online) This figure shows the integrand of equation (1) for the thirteen energy thresholds used at C-Mod and for three different electron temperatures. Notice the exponential dependence of the area under the each energy threshold curve which is proportional to the number of x-ray photons detected.

of 0.6 keV. The maximum measured average counts for a 10 ms integration time were of the order of 450 photons/ms indicating the pixels were below saturation which is  $1.0 \times 10^3$  photons/ms. The asymmetry in the count data across the different channels can be attributed to an approximate 10 degree angle of the center of the detector (and diagnostic port) to the toroidal plane of the plasma. The rapid decrease in counts for sight-lines which are not aligned with the core is due to the strong temperature and density sensitivity to soft x-ray emissions and the characteristic peakedness of the L- and H-mode discharges [again see Figure 6-a)]. The broadening seen at low-energies (e.g. for the 4-5 keV energy thresholds) of the H-mode case are likely not due to continuum emission but the strong recombination edge of Ar which is more prominent at lower temperatures found further away from the core [5, 22]. The signal-to-noise ratio decreases dramatically at lower temperatures and higher energy thresholds further increasing the error away from the magnetic axis.

## 6. Temperature Estimates

From the numerical fit of line-integrated brightnesses for energy thresholds between 6 and 15 keV it is possible to isolate the continuum emission and thus infer the weighted line-average electron temperature along each line of sight. As equation (1) suggests, the fitting routine to find local electron temperatures - and later the product of  $n_e n_Z$  - should be applied on the inverted local multi-energy SXR emissivities. However, the line-integrated brightness measurements are heavily weighted along the line of sight by a strong density ( $n_e^2$ ) and temperature dependence as shown also in equation (1) and the data in Figure 5. In most cases the line-integrated measurements are therefore a good *proxy* for the local emissivity at the distance of closest approach to the volume with the hottest and most dense plasma volume (e.g. plasma core). To check the consistency of the Maxwellian electron energy distribution function and the possible line-emission contamination, the ME-SXR signals should also be routinely plotted as a function of the respective threshold energies. If these basic assumptions are valid, the trace found should have an exponential dependence on energy as predicted by

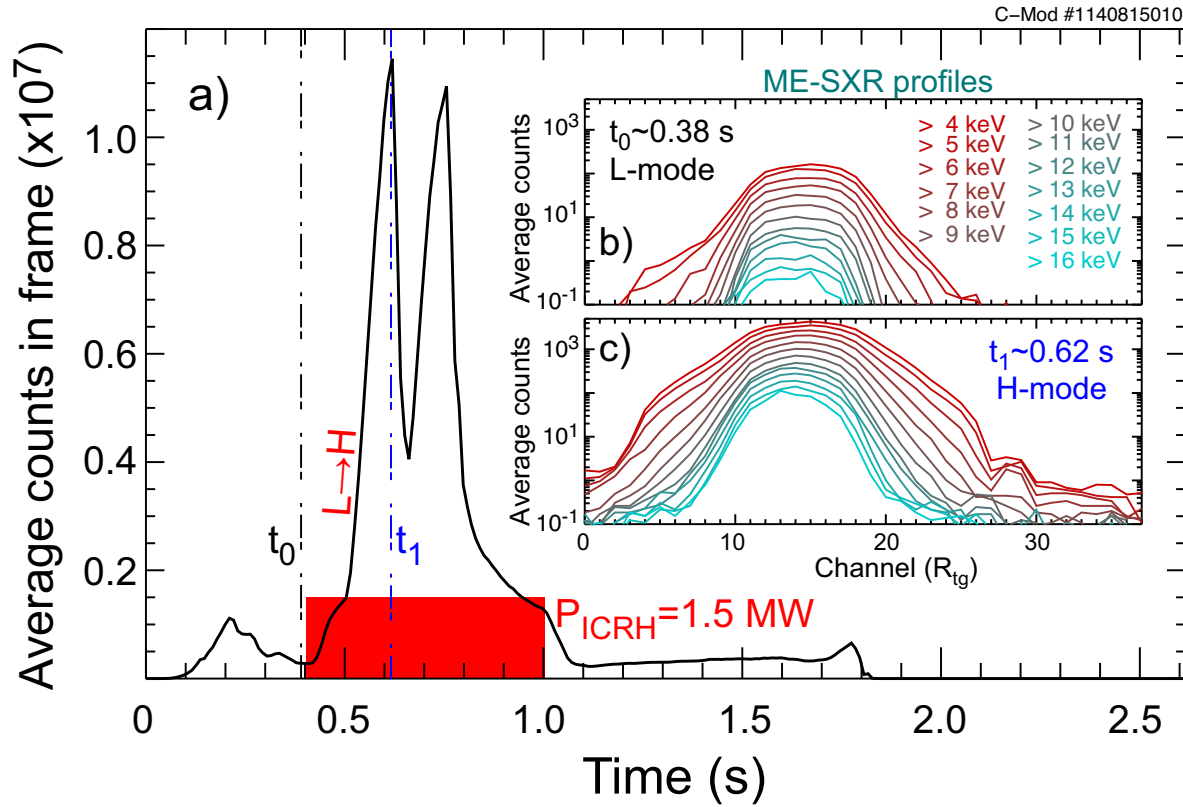


**Figure 6.** (Color Online) Total average x-ray counts for all channels over the length of the shot (a) and total average counts at different energy thresholds and across the channels of the detector for two different times, (b) and (c). The times of (b) and (c) are marked with vertical dotted line in (a).

the ideal solutions in equation (4).

However, in cases of strong inhomogeneities in the local plasma characteristics (e.g. caused by MHD activity and/or poloidal asymmetries due to centrifugal effects) or broader SXR emissivity profiles (e.g. as in the case of high-confinement H-modes), the limitations of the multi-energy fit using line-integrated signals rather than the local emissivity - becomes apparent and a tomographic inversion will become imperative. The analysis reported here focuses on the core plasma using the sightline with maximum x-ray counts seen in Figure 6 [see ch. # 14 in insets -b) and -c)]. The fits shown in Figure 7 correspond to the numerical solution of equation (2) and the ideal approximations used when calculating the number of x-rays and their power described by the equations in Section 4. These exponential-like fits provide a consistency check and proof that the measurement is not substantially contaminated by line emission and suprathermal electrons. Each functional or numeric best fit gives an estimation to the ‘line-averaged’ electron temperature. The exponential-integral and exponential solutions do not include the physics of the transmission along the detection chain, instead assuming that the electric response of the detector is described by a Heavyside function as opposed to the actual response, shown for instance in Figure 4.

The ME-SXR analysis provides here an accurate measurement of the dynamic evolution of the core electron temperature for nearly all the duration of the plasma discharges, including the ‘L-mode’ phase and the ICRH heating periods which transitioned into H-modes. By including the physics of the x-ray transmission as photons reach the detector and how they respond to absorption, the numeric solution gives an average line integrated electron temperature, heavily weighted by the core temperature and agrees closely with central ECE measurements.

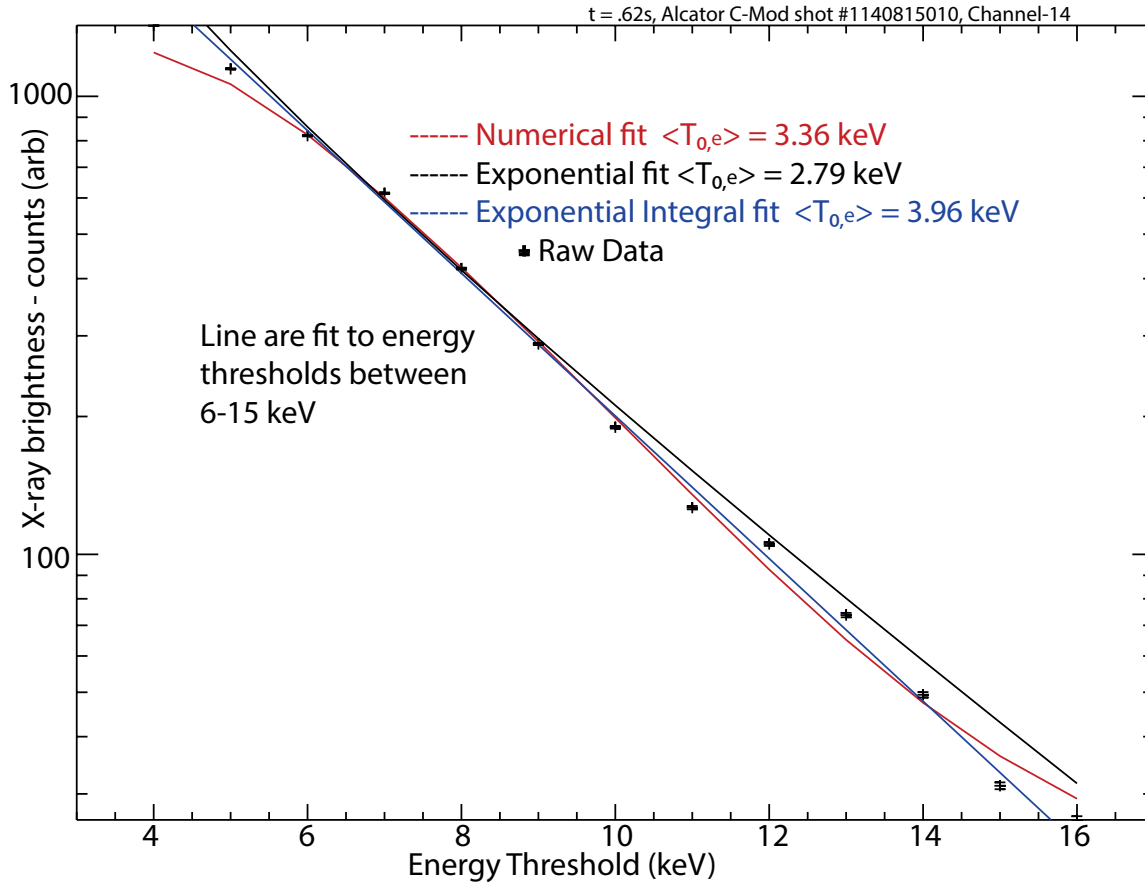


**Figure 7.** (Color Online) X-ray counts averaged, from channel 14, and plotted as a function of energy threshold. The fits represent different solutions which are considered. They strongly depend on electron temperature, and do not include the 4 keV and 5 keV points because of corruption from an Ar recombination edge and Ar and Mo line emissions, as seen in Figure 3.

During the brief transitions to the early H-modes the average temperature from the numeric fit captures most of the features of the temperature evolution even though its time-resolution is limited to 10 ms and cannot follow the temperature excursions due to core (1,1) sawteeth oscillations. Due to profile broadening and impurity peaking these measurements fail to take in account known systematic errors such as neglecting continuum recombination radiation and the energy dependent variation of the free-free gaunt factor. Nonetheless, this first results encourages further work to better account for systematic errors and inverting the brightness data to find local emissivity and temperature profiles.

Line-averaged temperature profiles can be determined by using the different channels or lines of sight of the detector. The electron temperature profile is plotted with corresponding ECE measurements in Figure 10. The two lines, seen in the figure, originate from the up-down asymmetry in the plasma, as viewed by the detector, this asymmetry emerges both from the tilt of the detector ( $\approx 10^\circ$ ) and the asymmetry in the plasma. This asymmetry further motivates a tomographic inversion to generate a symmetric profile and better understand the sources of asymmetry.

The ME-SXR line-integrated electron temperature profile follows ECE systems to within approximately 10%, which

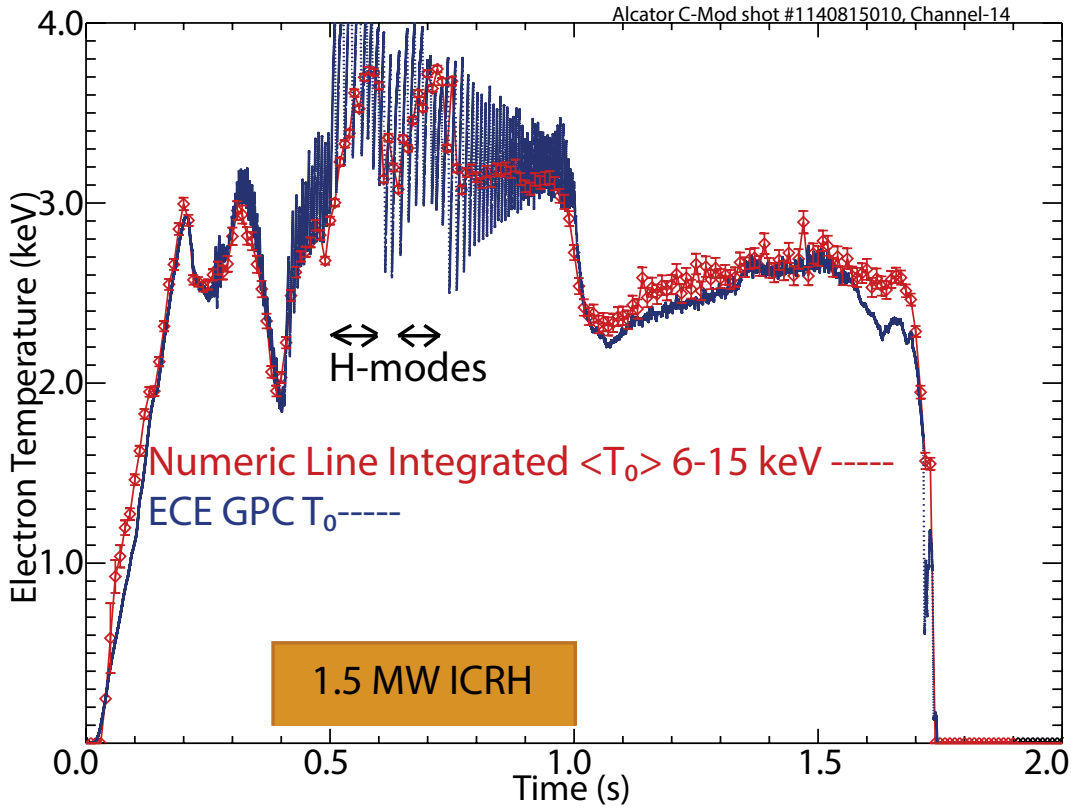


**Figure 8.** (Color Online) Near the beginning of shot, ICRH induces two separate L to H mode transition and rapid sawteeth in the ECE temperature data. The ‘average’ central electron temperatures from ME-SXR follows the ECE data within the temporal precision of 10ms.

is within the combined  $\sigma_{T_e(ECE)} \approx \sigma_{T_e(ME-SXR)} \approx 5-10\%$  error of each diagnostic. Although this error is not shown on the error bars it is expected when including systematic errors such as neglecting impurity density dependent recombination terms and the variation of the free-free gaunt factor depending on the energy of the photons, the temperature of the plasma, and the nuclear charge of the ion. Particularly the recombination term becomes more important with higher Mo and Ar impurity density.

## 7. Future Work

To better resolve the electron temperature profile the line integrated x-ray brightnesses can be tomographically inverted to calculate local emissivities. The inversion assumes constant emissivity across magnetic flux surfaces to generate emissivity profiles as a function of distance away from the magnetic axis. Assuming emissivity is a constant flux function requires that we assume electron temperature and impurity/electron density are also constant along flux surfaces. In addition, use of multiple systems would allow for 2D tomography without the need for this assumption [23].

Numerical ME-SXR analysis can also explore electron temperatures and impurities at higher  $T_e$  in tokamaks with

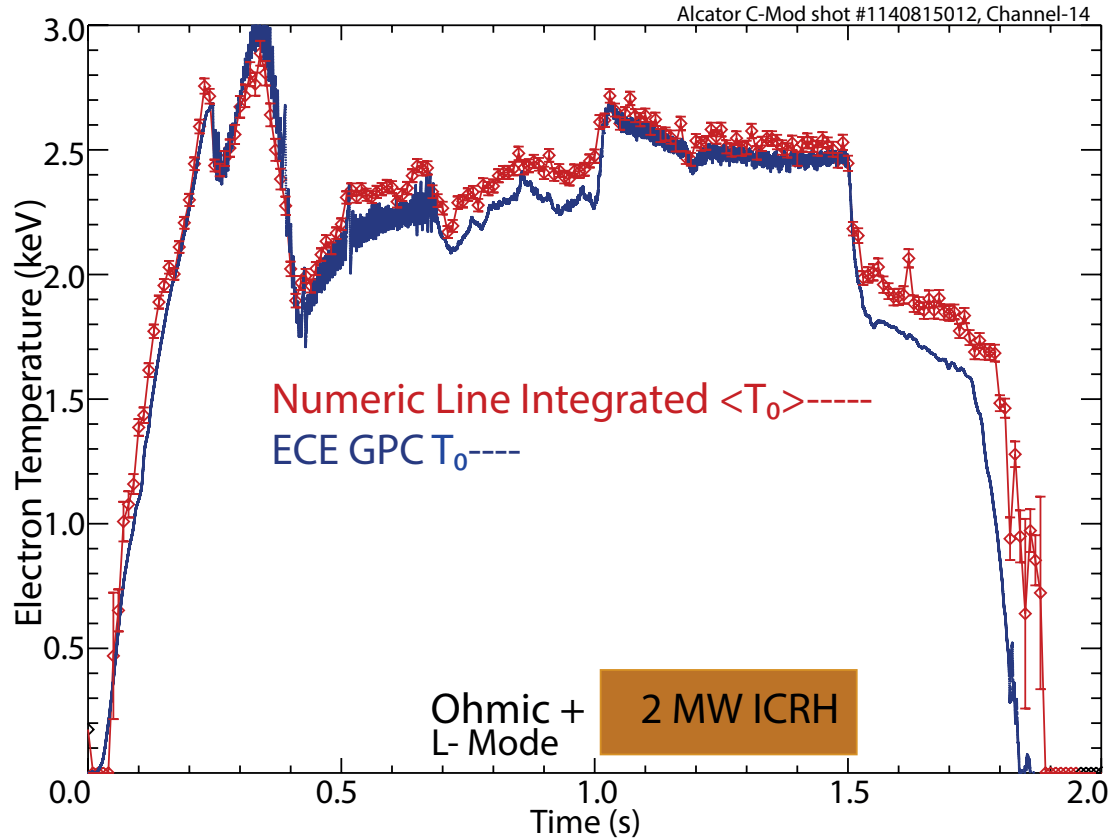


**Figure 9.** (Color Online) The electron temperature determined from central channel 14, at 10 ms intervals, and plotted for the duration of the plasma shot including ICRH in the latter half. The electron temperatures from ECE core  $T_e$  measurements are also plotted.

tungsten (W) walls. Tungsten is line free at higher energies 20-55 keV and at ITER temperatures bremsstrahlung emissions will be substantial. To improve statistics electron temperatures could be found from counts detected using this continuum energy range. The limitations of the absorption of Si detectors at these energies can be overcome with higher-Z semiconductors such as CdTe. Current CdTe detectors have 100% quantum efficiency for photons up till 60 keV [24]. Tungsten also has line emissions at lower energies which can be bracketed by lower energy thresholds to determine the degree in which W impurity enters the higher  $T_e$  plasma.

## 8. Conclusions

The dependence of continuum emissions on energy is used to find electron temperature. Variable energy x-ray imaging of high temperature plasmas provides an opportunity to measure  $T_e$  with minimum diagnostic footprint. Use of minimum

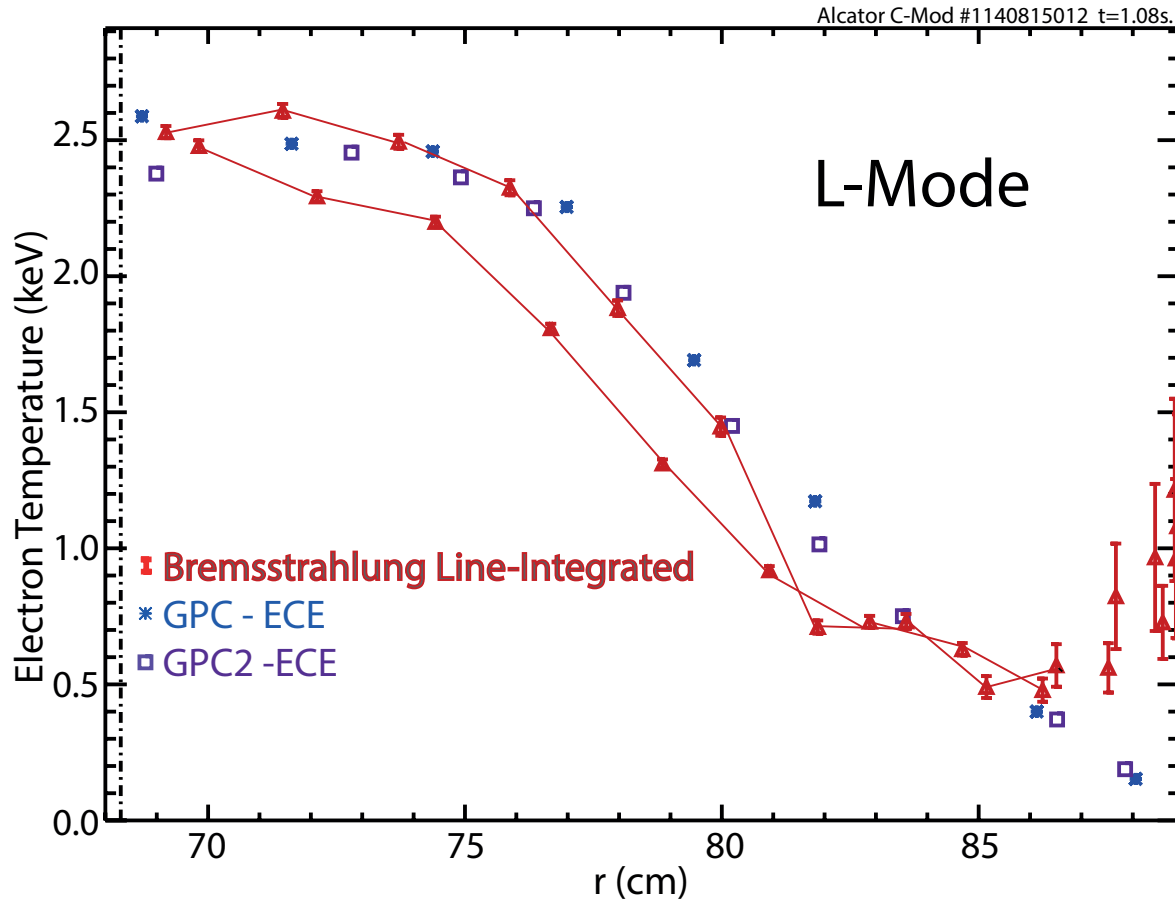


**Figure 10.** (Color Online) Soft X-ray average temperature profiles, across the viable channels of the Pilatus detector, compared to ECE temperature measurements at different radii, mapping all measurements to the outer midplane. The two lines emerge because of the asymmetry in the view of the detector, the tilt and plasma asymmetry both contribute.

energy thresholds allows for photon detection in specific energy ranges and allows separate access to continuum-emissions and characteristic lines. The detection of electron temperature from the continuum's energy slope reproduces every feature of central electron temperature in Ohmic and ICRH heating plasmas, as observed with the ECE diagnostic. New experiments will investigate the effect of impurities and non thermal tails in L, H and I-Mode plasmas with  $4 \lesssim T_{e,0} \lesssim 10$  keV and brighter higher energy emissions.

## Acknowledgements

This work was performed at Alcator C-Mod, a DOE Office of Science User Facility under US DoE contracts DE-FC02-99ER54512 at MIT and DE-AC02-09CH11466 at PPPL and support from US DOE Contract No.DE-AC02-09CH11466 and the DoE Undergraduate Laboratory Internship (SULI) program.

## References

- [1] V. V. Mirnov, *et al.*, Rev. Sci Instrum., **85**, 11D302, (2014)

- [2] Austin, M. E., Joint Workshop on Electron Cyclotron Emission and Electron Cyclotron Resonance Heating, **EC-15**. World Scientific Publishing Co. Pte Ltdp. 170-177., (2009).
- [3] L. Yong, *et al.*, Chin. Phys. B, **21**, 4, (2012).
- [4] S. Coda, *et al.*, Rev. Sci. Instrum., **79**, 10F501, (2008).
- [5] M. Diesso, K. W. Hill, *et al.*, Rev. Sci. Instrum. **59**, 08, 1760, (1986).
- [6] L. Delgado-Aparicio, D.Stutman, *et al.* Plasma Phys. Control. Fusion. **49**, p.1245-1257, (2007).
- [7] K. Tritz, *et al.*, Rev. Sci. Instrum., **83**, 83, (2012).
- [8] M. B. McGarry, *et. al.*, Rev. Sci. Instrum. **81**, 10E129, (2010)
- [9] P. Franz, *et. al.*, Nucl. Fusion, **53**, 5, (2013).
- [10] L. Delgado-Aparicio, *et al.*, Nucl. Fusion, **49**, 085028, (2009).
- [11] L. Delgado-Aparicio, K. Tritz, *et al.*, Rev. Sci. Instrum. **81**, 10E303, (2010).
- [12] D.Baiao, *et al.*, Rev. Sci. Instrum., **83**, 10E104, (2012).
- [13] Y.L Li, K. Tritz, *et al.*, Rev. Sci. Instrum., 123512, (2015).
- [14] N. A. Pablant, L. Delgado-Aparicio, *et al.*, Rev. Sci. Instrum. **83**, 10E526, (2012).
- [15] Pilatus Detection Systems User Manual. Version 1.3 Dectris., (2007).
- [16] M.L. Reinke, *et al.*, Rev. Sci. Instrum., **83**, 113504, (2012).
- [17] J. E. Rice, *et al.*, Phys. Rev. A, 53, 3953, 1996
- [18] FLYCHK: Generalized population kinetics and spectral model for rapid spectroscopic analysis for all elements, H.-K. Chung, M.H. Chen, W.L. Morgan, Yu. Ralchenko, and R.W. Lee, High Energy Density Physics v.1, 3, (2005).
- [19] J. Karzas and R. Latter, *et al.*, Astrophys. J. Suppl. S. **6**, 167, (1961).
- [20] B.L. Henke, E.M. Gullikson, and J.C. Davis. X-ray interactions: photoabsorption, scattering, transmission, and reflection at E=50-30000 eV, Z=1-92, Atomic Data and Nuclear Data Tables Vol. **54** (no.2), 181-342, (July 1993).
- [21] L. Delgado-Aparicio, D.Stutman, *et al.*, Journal of Applied Physics **102**, 073304, (2007).
- [22] J.E. Rice, *et al.*, Nucl. Fusion, **37**, 241, 1997
- [23] N. Pablant, *et al.*, Rev Sci Instrum. **85**, 11E424, 2014
- [24] L. Delgado-Aparicio, *et al.*, PPPL Report *Energy-resolved x-ray imaging for magnetically confined fusion plasmas: measurement of impurity concentration and thermal and non-Maxwellian electron distributions*, Report **4977**, <http://bp.pppl.gov/pubreport/2014/PPPL-4977.pdf>, (2014).

# Princeton Plasma Physics Laboratory Office of Reports and Publications

Managed by  
Princeton University

under contract with the  
U.S. Department of Energy  
(DE-AC02-09CH11466)

---

P.O. Box 451, Princeton, NJ 08543  
Phone: 609-243-2245  
Fax: 609-243-2751

E-mail: [publications@pppl.gov](mailto:publications@pppl.gov)

Website: <http://www.pppl.gov>